Design of High-Temperature Superconducting Dual-Band Filter With Multiple Transmission Zeros

Liguo Zhou ⬤, Hui Li ⬤, *Member, IEEE*, Zhihe Long ⬤, Shuangshuang Cao, Mingyan Jiang, and Tianliang Zhang ⬤, *Member, IEEE*

Abstract—A multiorder dual-band high-temperature superconducting (HTS) bandpass filter (BPF) with multiple transmission zeros (TZs) is designed in this paper. The theoretical characteristics of the introduction of TZs by the electric and magnetic mixed coupling and the cascade quadruplet (CQ) cross-coupling structures are analyzed, respectively. These two methods can be applied to the design of the multimode compact dual-band HTS BPF with controllable central frequency, bandwidth, and TZs. For demonstration, a Y-shape tunable resonator structure, which can simultaneously implement the internal electric and magnetic mixed coupling, and the external cross coupling are constructed to achieve the proposed dual-band BPF. The external quality factors required by the two passbands and the feasibility of independently adjusting the coupling strength between adjacent resonators are analyzed. Finally, a six-order dual-band HTS BPF with the center frequencies of 1490 (bandwidth of 40 MHz) and 2340 MHz (bandwidth of 80 MHz) is designed and fabricated on the double-sided YBCO/MgO/YBCO HTS thin films with the size of 17.2 mm × 14.7 mm ($0.20\,\lambda_g$ × $0.17\,\lambda_g$), and there are multiple of TZs located outside the two passbands, respectively. The out-of-band rejections are greatly improved to 70 and 80 dB due to these TZs, which fully exhibits the advantages of the proposed dual-band BPF. The measured results are in good agreement with the simulated ones.

Index Terms—Cascade quadruplet (CQ), dual band, high-temperature superconducting (HTS), passband filter, transmission zero (TZ).

I. INTRODUCTION

WITH the rapid development of communication industry, especially the wide application of wireless local area networks, multiband microwave systems that can be compatible with different communication resources have become one of the hotspots of research. As the key device of these communication front ends, the new technologies of the dual-band or multiband filter emerge one after another. In [1]–[18], the multiband bandpass filters (BPFs) designed based on a single multimode resonator are presented. Taking the
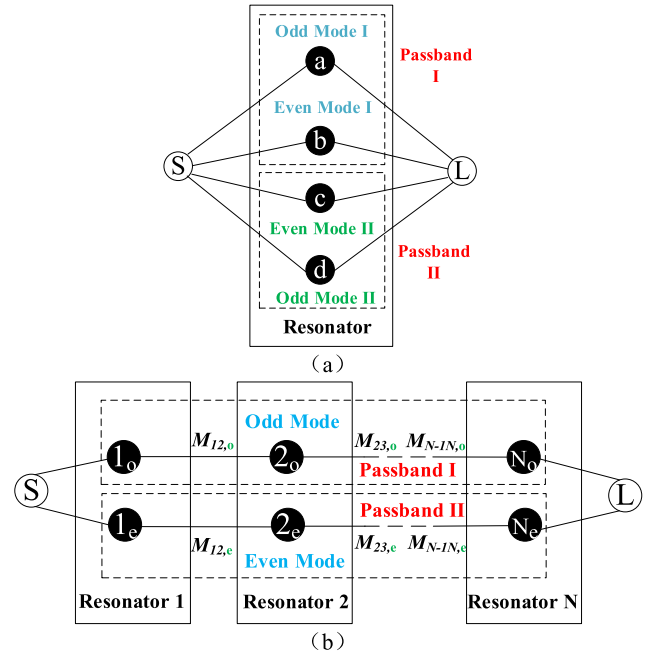
Fig. 1. Coupling schemes of dual-band BPFs. (a) Coupling scheme of single-order multimode dual-band BPFs. (b) Coupling scheme of multiorder multimode dual-band BPFs.

single-order multimode dual-band filter as an example, as shown in Fig. 1(a), the whole filter has only one resonator to realize two passbands by adjusting the resonant frequencies of different modes, so there is a great limitation in the bandwidth and the out-of-band suppression. The concrete structure forms of single-order multimode dual-band filter are as follows: the cavity multimode structure [1], the substrate integrated waveguide structure [2], [3], the lumped-element structure [4], [5], and the microstrip single-order multimode structure [6]–[18], etc., in which the single-order multimode resonator of the microstrip structure is widely used because of its simple configuration and small size. Each of the abovementioned structures has its own characteristics and advantages, but these structures have common shortcomings, such as the unsatisfying insertion loss in the passband and the suppression out of the passband, which are the two most important performance indicators of the filter itself, and these two features are usually contradictory. The high-temperature superconducting (HTS) material, cavity structure, and coplanar waveguide structure have some advantages on the insertion loss of the filter, so many papers will adopt these

structures, such as [19]. However, even though based on the HTS material, if the single-order structure is applied, the out-of-band rejection will still be unideal. For example, in [2], [3], and [6]–[19], the dual-band filters based on the single-branch resonator, the stepped-impedance resonator, and the half-wavelength or quarter-wavelength resonator are all designed with only one resonator.

In order to solve the abovementioned problems, the multi-order multimode filter is proposed by applying the theory of single-order multimode filter into the multiorder filters parallel theory. In [20]–[24], the two-order multimode dual-band BPFs are designed, and their out-of-band rejections are improved significantly compared with single-order ones'. In [24]–[36], the multiorder multiband BPFs are implemented based on the multiorder filter theory of microstrip structure, and the superconducting material is used in [21], [23], [24], [26], and [28]–[34]. Fig. 1(b) shows an N-order dual-band coupling prototype, which consists of N resonators with separated odd and even modes. All the odd modes are coupled together to form a passband, and the other passband is composed of all the coupled even modes. The adjacent resonators with different modes are coupled by independent coupling coefficients $M_{ij,o}$ and $M_{ij,e}$. $M_{ij,o}$ represents the odd-mode coupling coefficients between resonators i and j. $M_{ij,e}$ indicates the even-mode coupling coefficients between resonators i and j.

In recent years, with the development of HTS materials and the stability of processing technology, the design of HTS multiorder microstrip structure filters is increasingly prevalent. Because the HTS thin film possesses very low microwave surface resistance and extremely high Q value, the multiorder single-band BPF based on it can have excellent band-edge characteristics, out-of-band suppression, and insertion loss. The multiband filter based on the HTS materials can also present these remarkable advantages, and as mentioned before, the dual-band filters in [21], [23], [24], [26], and [28]–[34] are all realized by HTS technology. The advantages and technical difficulties of the HTS dual-mode dual-band filter have been summarized in [24] and [28]. In [24] and [33], the multiband filter configurations cannot realize the independent control of each passband bandwidth, because there only exists one distance variable between adjacent resonators, if it is tuned, the coupling coefficients in all passbands will be changed together.

In this paper, a HTS dual-band BPF with independent controllable central frequencies and bandwidths is presented. Moreover, multiple of controllable transmission zeros (TZs) is situated outside each passband, which is introduced by the cross-coupling structure and electric magnetic mixed coupling, respectively. The remainder of this paper is organized as follows. In Section II, the structure of Y-shape folded tunable resonator and the modal resonant characteristics are introduced. Based on this structure, the coupling characteristics between adjacent resonators and the realization of the external quality factor are also given. Section III mainly analyzes the two methods of introducing the TZs, i.e., the electric magnetic mixed coupling and the cross-coupling approaches, and the characteristics of these two methods applied in the design of dual-band filters are summarized as well. Then, a dual-band BPF is designed based on the
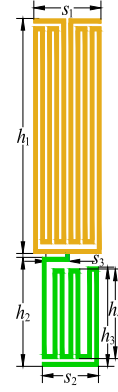

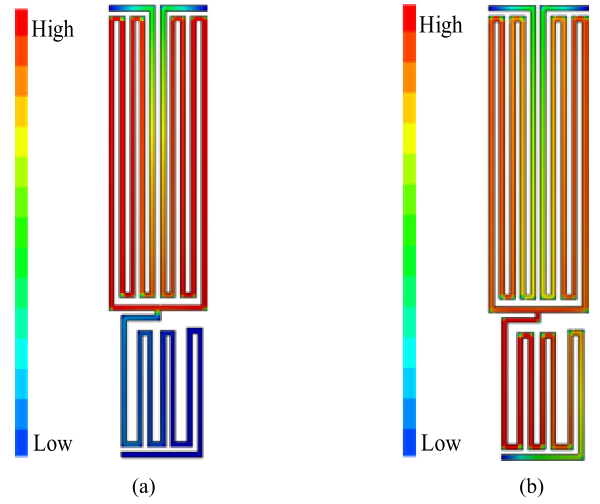Fig. 2.   Proposed Y-shape folded tunable resonator.

Fig. 3.   Current distribution simulation of Y-shape folded tunable resonator. (a) Current distribution simulation at f_o. (b) Current distribution simulation at f_e.

Y-shape folded tunable resonator. Section IV mainly introduces the fabrication and measurement of HTS dual-band filter with multiple TZs.

II. Y-SHAPE FOLDED TUNABLE RESONATOR

A. Y-Shape Folded Tunable Resonator Structure and Control of Resonant Frequencies

Fig. 2 shows the microstrip structure resonator designed in this paper, named Y-shape folded tunable resonator. To facilitate the subsequent description, the dual-mode resonator is divided into the yellow microstrip part and the green microstrip part. The length and width of the yellow microstrip part are expressed by h_1 and s_1. The length and width of the green microstrip part are expressed by h_2 and s_2, and h_3 and h_4 are added to indicate the other microstrip lines that are different from h_2.

The Y-shape folded tunable resonator is designed on a MgO substrate with a thickness of 0.5 mm and a dielectric constant of 9.8, and the full-wave current characteristic of the resonator is simulated, as shown in Fig. 3, in which Fig. 3(a) and (b) shows the current density distributions at the frequencies of f_o and f_e (f_o and f_e are the frequencies of odd mode and even mode),

respectively. According to Fig. 3, when using f_o as the simulation frequency, the current energy is mainly concentrated in the upper part (yellow microstrip part of resonator shown in Fig. 2). However, when f_e is the simulation frequency, the current energy is distributed relatively evenly in the whole resonator. So, the resonant frequency f_o is only related to the yellow microstrip part shown in Fig. 2, and the resonant frequency f_e has to do with the entire Y-shape folded tunable resonator.

According to the multimode transmission line theory, the Y-shape folded tunable resonator is a typical half-wavelength ($\lambda/2$) resonator when the resonant frequency f_o is realized, and the green microstrip part of Fig. 2 can be equivalent to the open circuit microstrip structure under this situation. Similarly, the Y-shape folded tunable resonator is a typical half-wavelength ($\lambda/2$) resonator when the resonant frequency f_e is achieved. In the case of the resonant frequency f_e, the symmetrical microstrip lines about the vertical axis in the yellow microstrip part is a parallel structure, which is then in series with the microstrip line of the green microstrip part, and finally the half-wavelength resonator is formed, which can be treated as a stepped-impedance structure model. The resonant frequencies (f_o and f_e) of these two cases can be expressed by (1) and (2), respectively, where the parameters h_i and s_i represent the length and width of the transmission lines shown in Fig. 1. c represents the speed of light in the vacuum, and the dielectric constant of the substrate is expressed by ε_{eff}. It is worth noting that when the resonant frequency is f_e, the electric length of the half-wavelength resonator can be calculated equivalently through the stepped-impedance model. From the following two equations, it can be also known that f_o is only related to h_1 and s_1, and f_e is associated with all the annotated dimensions shown in Fig. 2:

$$f_o \approx \frac{c}{(20h_1 + 4s_1)\sqrt{\varepsilon_{\text{eff}}}} \tag{1}$$

$$f_e \approx \frac{c}{(10h_1 + 2s_1 + s_3 + h_2 + 2s_2 + 2h_3 + 4h_4)\sqrt{\varepsilon_{\text{eff}}}}. \tag{2}$$

Under the weak-coupling condition, the frequency response of the resonator is analyzed. In this paper, the widths of the lines and slots of the resonator are all 0.1 mm. When s_1, s_3, and s_2 are fixed at 1.90, 0.56, and 1.58 mm, respectively, and $h_1 = 6.00$ and $h_2 = 2.80$ mm ($h_4 = 2.20$ and $h_3 = 2.54$ mm) or $h_1 = 6.10$ and $h_2 = 2.80$ mm ($h_4 = 2.20$ and $h_3 = 2.54$ mm) or $h_1 = 6.10$ and $h_2 = 3.00$ mm ($h_4 = 2.40$ and $h_3 = 2.74$ mm), the frequency response curves of the Y-shape folded tunable resonator are shown in Fig. 4(a). It is worth mentioning that h_3 and h_4 would be changed with the change of h_2. As seen from Fig. 4(a), when h_1 changes from 6.0 to 6.1 mm and h_2 remains unchanged at 2.8 mm, both f_o and f_e move to low frequency, which means the length of h_1 affects f_o and f_e simultaneously. Similarly, with the change of h_2 from 2.8 to 3.0 mm and h_1 remaining unchanged at 6.1 mm, f_o remains stationary, whereas f_e shifts to low frequency, so the length of h_2 only influences f_e without affecting f_o, which are consistent with the expression of (1) and (2). In order to further facilitate the adjustment of resonant frequency f_e, h_4 can also be used to the fine tuning of
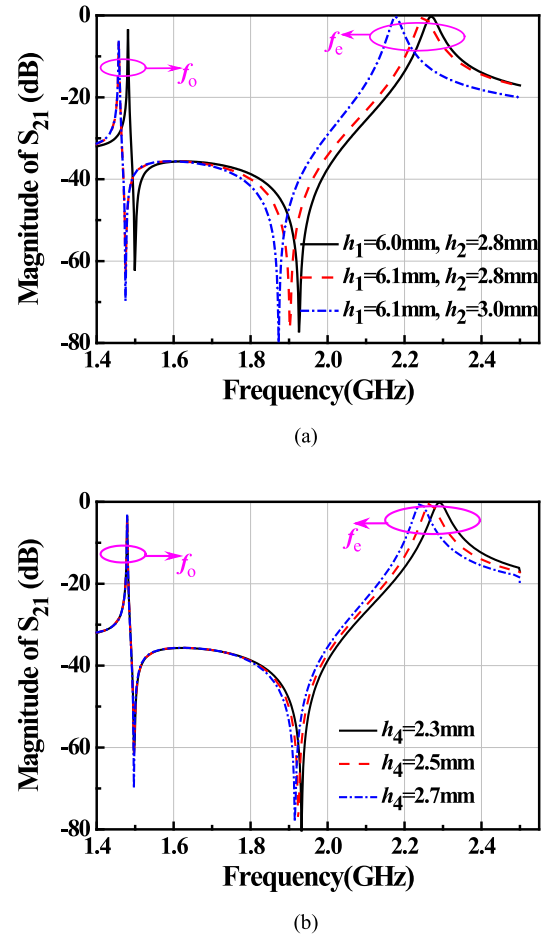

Fig. 4. Modal resonant characteristics with varied microstrip line lengths. (a) With varied h_1 and h_2, as shown in Fig. 1. (b) With varied h_4, as shown in Fig. 1.

the position of f_e, addition the relationship between the resonant frequencies (f_o and f_e) and h_4 is depicted in Fig. 4(b).

In summary, the central frequencies of the two passbands can be determined as follows: First, by adjusting the length h_1 of the yellow microstrip part shown in Fig. 2, the required f_o can be obtained. Then, with h_1 unchanged (f_o is not affected), through tuning the length h_2 of the green microstrip part, the desired f_e can be controlled. Finally, f_e can be accurately adjusted by a slight change of h_4. Based on this adjustment order, the control of both central frequencies of the two passbands can be achieved.

B. Filter Bandwidth Adjustment Based on Y-Shape Resonator

Based on the Y-shape resonator structure proposed above, two kinds of coupling modes can be formed by two coupled Y-shape resonators, as shown in Fig. 5(a) and (b), which are defined as Type I and Type II coupling types, respectively. For the yellow microstrip part shown in Fig. 2 that controls f_o, its structure is symmetrical about the vertical axis, so these two coupling types are the same, but for the whole resonator that realizes f_e, Type I is different from Type II because the structure of the green microstrip part is asymmetrical. Fig. 6(a) and (b) shows the frequency response curves corresponding to
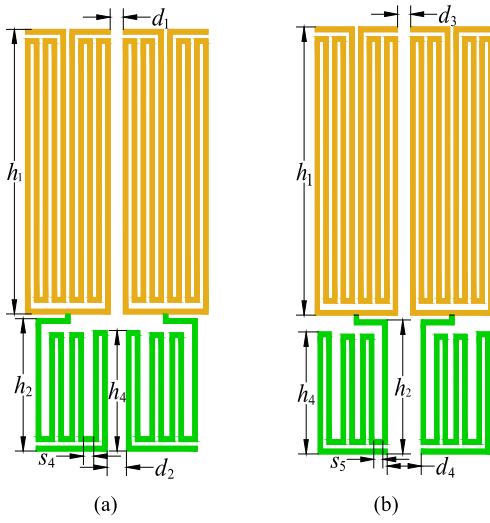
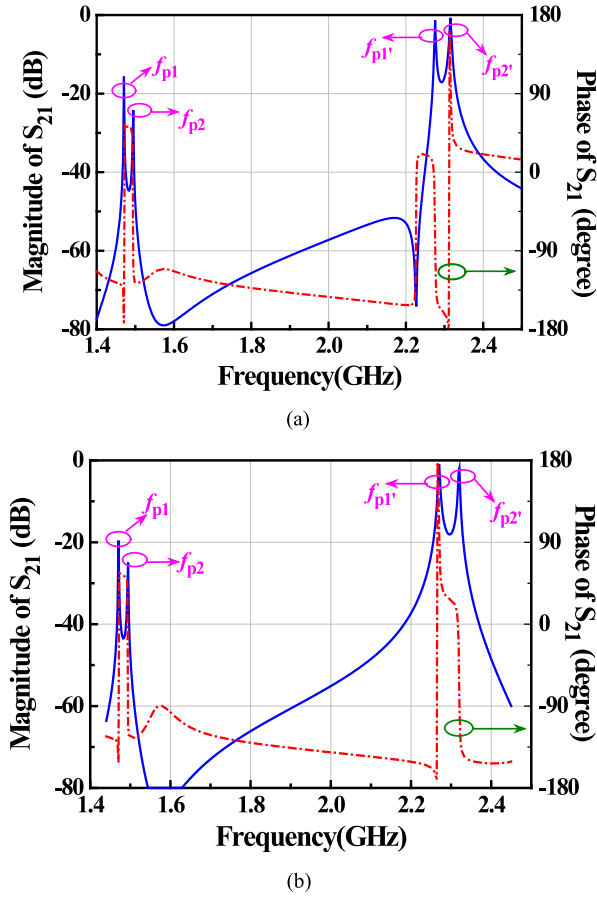Fig. 5.   Two kinds of coupling types. (a) Type I. (b) Type II.

Fig. 6.   Magnitude and phase responses. (a) Type I. (b) Type II.

the coupling structures of Type I and Type II, respectively, with $d_1 = 0.29$ mm, $h_1 = 6.00$ mm, $h_2 = 2.80$ mm, $d_2 = 0.43$ mm, $h_4 = 2.54$ mm, $s_4 = 0.23$ mm, $d_3 = 0.29$ mm, $s_5 = 0.20$ mm, and $d_4 = 0.78$ mm.

In Fig. 6(a), S_{21} shows the magnitude characteristic of S-parameters when two resonators are under the condition of weak external coupling, and there are two obvious resonant peaks at

both high frequency and low frequency, marked with f_{p1} and f_{p2}. f_{p1} and f_{p2} close to f_o are equal to 1470 and 1490 MHz, respectively. f_{p1} and f_{p2} near f_e are 2275 and 2315 MHz, respectively, and the TZ is located in 2227 MHz. In Fig. 6(b), the frequencies of f_{p1} and f_{p2} close to f_o are the same as those shown in Fig. 6(a), whereas f_{p1} and f_{p2} near f_e are 2270 and 2320 MHz, respectively. From (3), we know that the coupling strength between two resonators can be expressed by the coupling coefficient $m_{i,j}$, which can be computed by the locations of two resonant peaks as

$$m_{i,j} = \frac{f_{p2}^2 - f_{p1}^2}{f_{p2}^2 + f_{p1}^2}. \tag{3}$$

The phase response curves of the two coupling types are also shown in Fig. 6. According to the variations of the phase at the frequencies of the two resonances, it can be seen that at the first passband, the coupling modes of Type I and II are both magnetic coupling; at the second passband, the coupling mode between two resonators of Type I belongs to electric coupling and that of Type II are magnetic coupling. So, the two coupling types shown in Fig. 5 have no influence on the electric and magnetic coupling mode of the first passband, whereas they have an effect on that of the second passband, which can provide a flexible way for the introduction of TZs.

Under the weak-coupling condition, the relationship between the multiple distance variables of the adjacent coupled resonators in the two kinds of coupling types is shown in Fig. 5 and the coupling coefficient is analyzed, as shown in Fig. 7. The coupling coefficients between two resonators are obtained by (3). When d_2 is equal to 0.30 or 0.35 or 0.40 mm by adjusting s_4 shown in Fig. 5(a) and d_1 is used as the variable, the coupling coefficients between two resonators are changed as shown in Fig. 7(a), in which the curves corresponding to the odd modes and the even modes are expressed by Band I and Band II, respectively. The coupling coefficients of Band I decrease with the increase of d_1, and the coupling coefficients of Band I are identical when d_2 takes different values. The three coupling coefficient curves coincide, indicating that the coupling coefficients of Band I are not affected by d_2. The coupling coefficients of Band II increase with the increase of d_1 (this anomaly is related to the electric and magnetic mixed coupling, which would be explained in Section III), and the smaller d_2 is, the greater the coupling coefficients of Band II are, which shows that Band II is influenced by d_1 and d_2 simultaneously. In the same way, when d_2 is selected as the variable in the Type I of Fig. 5 and s_4 is adjusted to make d_1 equal to 0.20, 0.25, and 0.30 mm, respectively, the variations of the coupling coefficients between the two resonators are shown in Fig. 7(b), from which it can be observed that d_2 has no effect on Band I, whereas d_1 has an impact on both the coupling coefficients of Bands I and II. Similarly, with d_3 as the variable in Type II and d_4 tuned to be 0.30, 0.35, and 0.40 mm, respectively, the changes of the coupling coefficients between the two resonators are shown in Fig. 7(c), where the coupling coefficients of Bands I and II decrease with the increase of d_3, and when d_4 takes different values, the coupling coefficients corresponding to Band I are the same, whereas
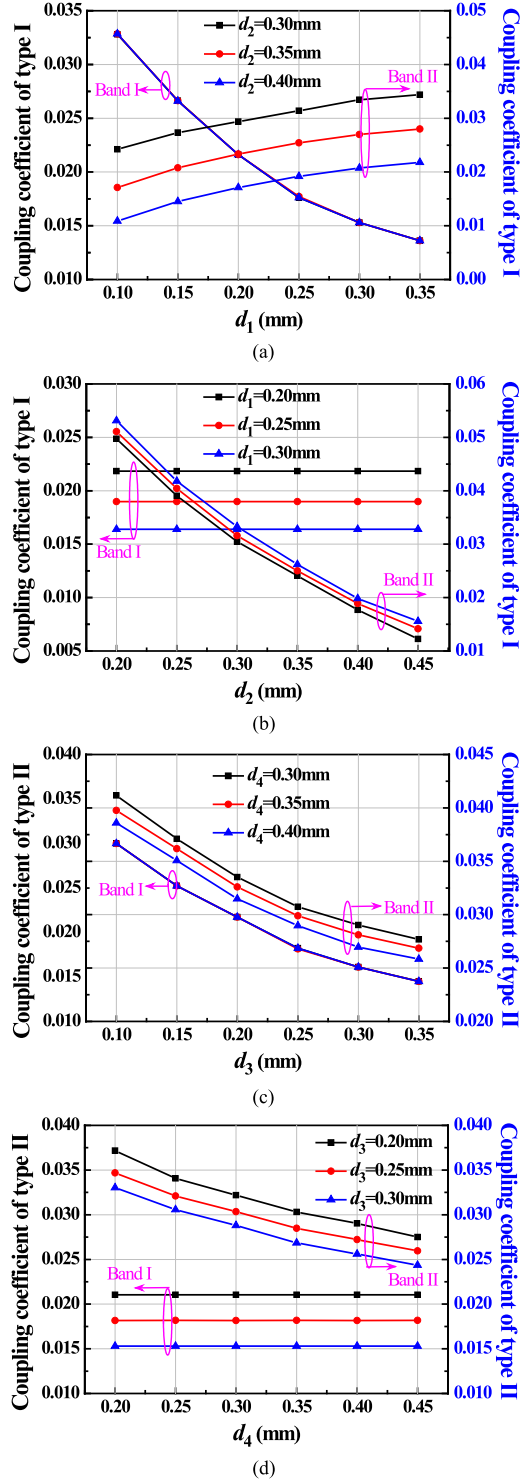
Fig. 7. Corresponding coupling coefficients as a function of coupling space. (a) Coupling space d_1. (b) Coupling space d_2. (c) Coupling space d_3. (d) Coupling space d_4.

Fig. 8. Y-shape resonator with tapped line structure.

by d_4, but the coupling coefficients of Bands I and II are both affected by d_3.

In conclusion, the coupling coefficients of Band I is inversely proportional to the distance between the two yellow microstrip parts shown in Fig. 5 regardless of Type I or II, and has nothing to do with the distance between the two green microstrip parts, while Band II is controlled by the coupling distance between the two whole resonators.

C. Analysis of External Quality Factor of Filter Based on Y-Shape Resonator

The two passbands with different fractional bandwidths of the dual-band filter have different demands on the external quality factor. In order to realize the flexible adjustment of the external quality factor of the two passbands, this section designs a coupling method using the tapped line structure based on the Y-shape resonator, as shown in Fig. 8. The two blue parallel microstrip lines are loaded on both the yellow and green microstrip parts of the resonator, and the other ends of these two blue microstrip lines connected together as an external input port to connect directly with the microwave connector. According to the previous analysis of the current characteristics of the Y-shape resonator, for the location of the external feeding line, the influence of the tapped line on the yellow microstrip part on the external quality factor of Band I is obvious, and the loading position of the tapped line on the green microstrip part has a

the coupling coefficients of Band II decreases with the increase of d_4. When d_4 is taken as the variable in the Type II and d_3 is chosen to be 0.20, 0.25, and 0.30 mm, respectively, the changing curves of the coupling coefficients between the two resonators are exhibited, as shown in Fig. 7(d), where Band I is not affected
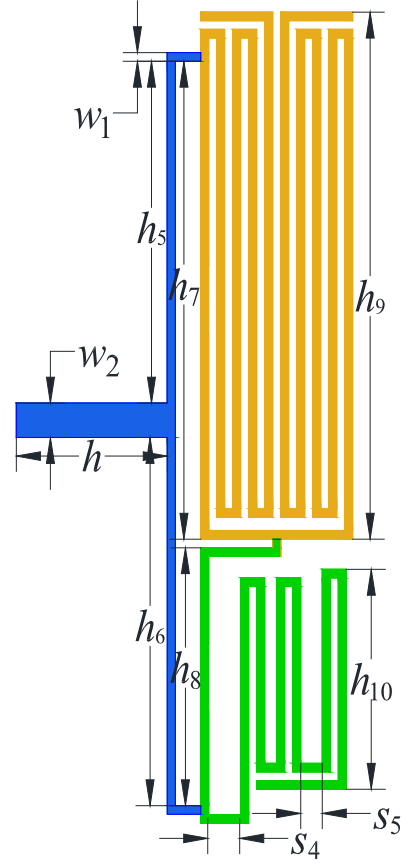
notable impact on the external quality factors of both Bands I and II. The external quality factor Q_e can be extracted through (4), where f_0 and $\Delta f_{3\text{-dB}}$ indicate the center frequency and 3-dB bandwidth, respectively, as

$$Q_e = \frac{f_0}{\Delta f_{3\text{-dB}}}. \tag{4}$$

When $h_7 = 5.5$ mm, $h_5 = 4.0$ mm, $w_1 = 0.1$ mm, and $w_2 = 0.4$ mm and remain unchanged, the external quality factors (Q_{e1} and Q_{e2}) of Bands I and II vary with the change of h_8, as shown in Fig. 9(a). When $h_8 = 3.0$ mm and $h_6 = 4.2$ mm and remain unchanged, Fig. 9(b) indicates the variations of Q_{e1} and Q_{e2} with varied h_7, where it can be seen that as h_7 increases, the external quality factor (Q_{e1}) of Band I decreases, whereas the external quality factor (Q_{e2}) of the Band II remains almost the same. From Fig. 9(a) and (b), it can be summarized that Q_{e1} is affected by both h_7 and h_8, and Q_{e2} is only affected by h_8, so that the two passbands' external quality factors can be tuned independently. Because $h_7 + h_8 + 0.1 = h_5 + h_6 + 0.4$, so when h_7 and h_8 are determined, h_5 and h_6 can also be set as tuning variables. Fig. 9(c) illustrates the changing curves of the external quality factors (Q_{e1} and Q_{e2}) of Bands I and II, which varies with the change of h_5. If the tapped line with length of h moves upward (h_5 becomes smaller), Q_{e1} gets smaller. Conversely, Q_{e2} decreases as the tapped line moves downward. According to the abovementioned relationship between the external quality factors and the loaded parallel microstrip feed lines, the required external quality factors (Q_{e1} and Q_{e2}) can be obtained. The adjustment process can be summarized as follows: First, h_8 is adjusted based on Fig. 9(a) to meet Q_{e2} of Band II, and then appropriate Q_{e1} of Band I can be achieved by tuning h_7. Lastly, h_5 can be used for further fine tuning of Q_{e1} and Q_{e2}.

III. INTRODUCTION OF TZs

As the spectrum resources get more and more crowded, the communication systems put forward higher requirements for the performance of the filters, especially the rectangular coefficient. The traditional Butterworth and Chebyshev filters have been difficult to satisfy the demands and so are the dual-band filters. In the design of filter, the quasi-elliptic function is usually adopted to achieve the introduction of finite TZs to improve the selectivity of passband, which has been widely studied in [37]–[41]. The following two typical methods would be applied to realize the quasi-elliptic function in this paper: controllable electric and magnetic mixed coupling and cross coupling.

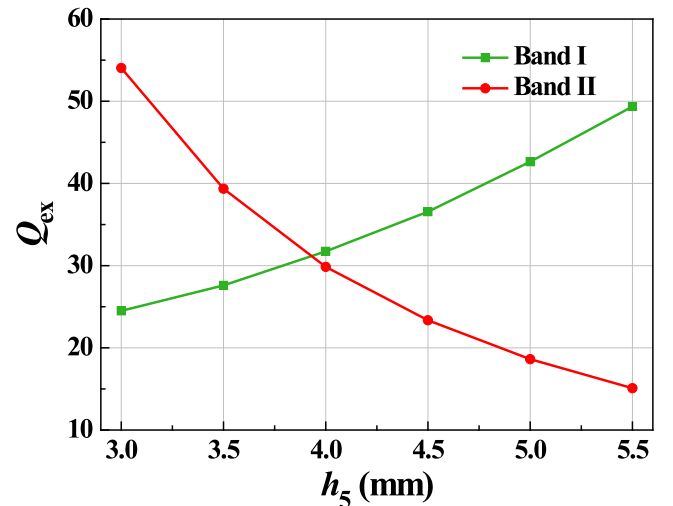### A. Controllable Electric and Magnetic Mixed Coupling to Introduce TZs

The study of controllable electric magnetic mixed coupling is given in [42]–[45]. By using the equivalent circuit with J inverters and combining the filter's LC lumped-element circuit and the relationship between the odd-mode resonant frequency ω_{od} and the even-mode resonant frequency ω_{ev}, the extraction equations of the magnetic coupling coefficient M_c, the electric coupling coefficient E_c, and the total coupling coefficient $m_{i,j}$ can be obtained, as expressed in (5)–(7), respectively, where ω_o
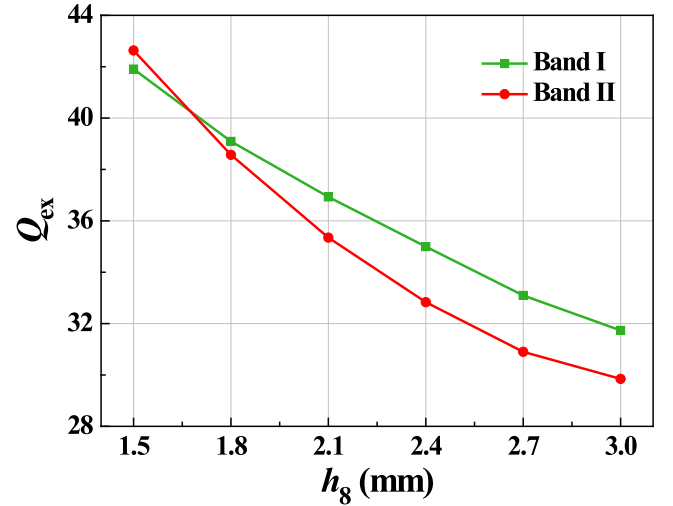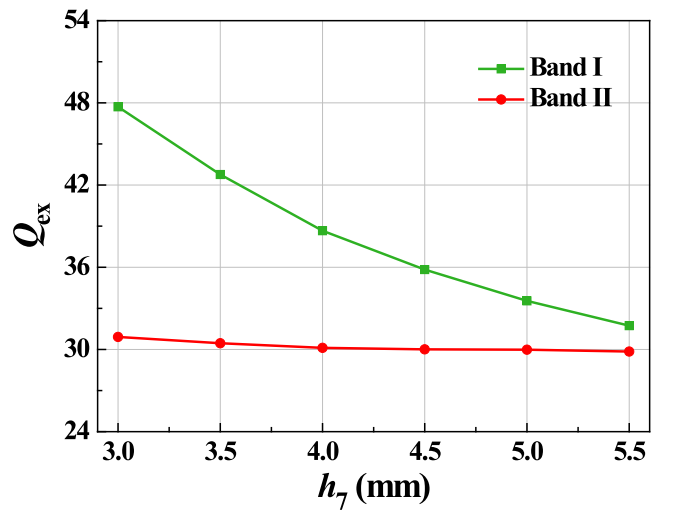
Fig. 9. External quality factors Q_{ex} as a function of coupling length. (a) Length of h_8. (b) Length of h_7. (c) Length of h_5.
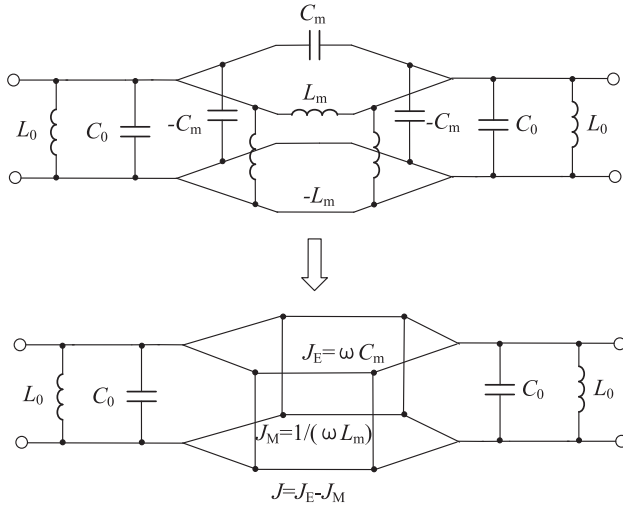
Fig. 10. Equivalent circuit of the electric and magnetic mixed coupling resonators indicated by the J inverter.

is the self-resonant frequency of the resonator and ω_m represents the frequency of TZ. Fig. 10 depicts the equivalent circuit of the electric and magnetic mixed coupling resonators by the J inverter.

$$E_C = \frac{\omega_{ev}^2 - \omega_{od}^2}{\omega_{ev}^2 + \omega_{od}^2 - 2\omega_m^2} \tag{5}$$

$$M_C = \frac{\omega_m^2 \left(\omega_{ev}^2 - \omega_{od}^2\right)}{2\omega_{ev}^2 \omega_{od}^2 - \omega_m^2 \left(\omega_{ev}^2 + \omega_{od}^2\right)} \tag{6}$$

$$m_{i,j} = \frac{J_E}{\omega_0 C_0} - \frac{J_M}{\omega_0 C_0} = \frac{C_m}{C_0} - \frac{L_0}{L_m}$$
$$= E_C - M_C = \frac{\omega_{od}^2 - \omega_{ev}^2}{\omega_{od}^2 + \omega_{ev}^2}. \tag{7}$$

According to the definitions of the electric and magnetic couplings, we get

$$\frac{M_C}{E_C} = \frac{L/L_m}{C_m/C} = \frac{LC}{L_m C_m} = \frac{\omega_m^2}{\omega_0^2}. \tag{8}$$

It can be seen from (8) that the ratio of the electric coupling coefficient and magnetic coupling coefficient determines the relative position between the self-resonant frequency ω_0 and the TZ frequency ω_m, and the closer the electric coupling and magnetic coupling coefficients are, the closer TZ is to the self-resonant frequency. The more direct equation can be expressed by the simplified (9), which can show the relationship between the electric coupling and magnetic coupling coefficients and TZs more simply as

$$f_z = f_0 \sqrt{\frac{M_C}{E_C}} \tag{9}$$

According to the coupling structure shown in Fig. 5(a) and the current density distribution analysis shown in Fig. 3, the coupling property of Band II formed by even modes is electric and magnetic mixed coupling and its coupling coefficient satisfies (7). The coupling property of the coupling type shown
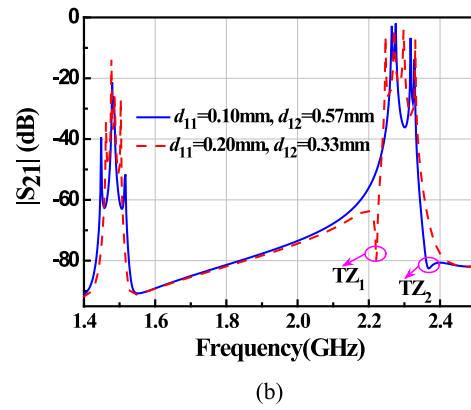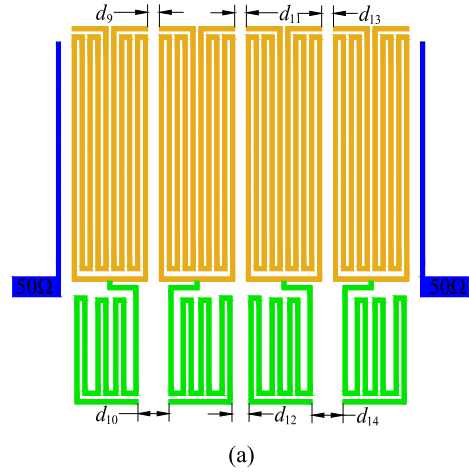

(a)

(b)

Fig. 11. (a) Multiorder electric and magnetic mixed coupling structure. (b) Frequency responses.

in Fig. 5(a) presents electric coupling ($m_{i,j} \leq 0$). As the d_1 value increases with d_2 fixed, the magnetic coupling between the yellow microstrip parts shown in Fig. 5(a) decreases, and the electric coupling strength between the green microstrip parts is unchanged, so the total coupling strength is stronger, which can be proved in the analysis shown in Fig. 7(a). Due to $M_c/E_c < 1$, a TZ near the low-frequency band of Band II can be generated based on (9). However, according to the frequency response shown in Fig. 6(a) of Fig. 5(a), when d_2 increases and d_1 decreases, the magnetic coupling increases and the electric coupling decreases, therefore based on (7), when the magnetic coupling is greater than the electric coupling, the total coupling shows the magnetic coupling. Due to $M_c/E_c > 1$, a TZ near the high-frequency band of Band II can be created based on (9).

The four-order electric and magnetic mixed coupling configuration is shown in Fig. 11(a). Based on the previous analysis of the coupling types shown in Fig. 5, for Band II, the coupling properties from left to right are the magnetic coupling, electric magnetic mixed coupling, and electric coupling, respectively. When d_{11} and d_{12} take different values, the total coupling characteristics would be varied, and the frequency responses are shown in Fig. 11(b) with $d_{11} = 0.2$ and $d_{12} = 0.33$ mm and $d_{11} = 0.1$ and $d_{12} = 0.57$ mm. Therefore, by reasonably adjusting the values of d_{11} and d_{12}, TZs can be generated. And according

to the actual specifications, TZs can be situated at either the high-frequency band or the low-frequency band.

B. Cross Coupling to Introduce TZs

The principle of introducing TZs by the cross-coupling structure filter is that the cross coupling is introduced between the nonadjacent resonators of the filter, which makes the signals have multiple transmission paths from the filter's input to the output, so that the 180° phase difference can be realized to create TZs through controlling the phases of different transmission paths.

The frequently-used cross-coupling structures are cascaded trisection (CT) and cascade quadruplet (CQ). For example, various conditions of the cross-coupling CT structure to introduce TZs are described in [46]. And a theoretical analysis of the CQ structure is presented in [47]. The analysis of TZs is summarized as follows: a typical transfer function is expressed by (10), where Ω is the normalized roll-off frequency variable of the lowpass filter. The relationship between the ripple coefficient ε and the return loss L_R in the passband is shown in (11), and the expression of $F_n(\Omega)$ is presented in (12). $\Omega = \pm\Omega_a \, (\Omega_a > 1)$ are the frequency locations of a pair of attenuation poles. The bandpass transmission frequency response is obtained by (13), in which ω is the frequency variable of the bandpass filter (BPF), ω_o is the central frequency of the BPF, and FBW is the fractional bandwidth of the filter.

$$|S_{21}(\Omega)|^2 = \frac{1}{1 + \varepsilon^2 F_n^2(\Omega)} \tag{10}$$

$$\varepsilon = \frac{1}{\sqrt{10^{-\frac{L_R}{10}} - 1}} \tag{11}$$

$$F_n(\Omega) = \cosh\left\{(n-2)\cosh^{-1}(\Omega) + \cosh^{-1}\left(\frac{\Omega_a\Omega - 1}{\Omega_a - \Omega}\right)\right.$$
$$\left. + \cosh^{-1}\left(\frac{\Omega_a\Omega + 1}{\Omega_a + \Omega}\right)\right\} \tag{12}$$

$$\Omega = \frac{1}{\text{FBW}} \cdot \left(\frac{\omega}{\omega_0} - \frac{\omega_0}{\omega}\right). \tag{13}$$

According to (10)–(13), a pair of finite TZs can be obtained and expressed by ω_{a1} and ω_{a2}, and the corresponding extracted expressions are shown as (14a) and (14b). When Ω_a takes different values, the frequency response of quasi-elliptic functions with different out-of-band suppressions can be realized [47]. It can be known that a pair of TZs is distributed symmetrically on both sides of ω_0, which can be obtained by the CQ coupling structure, from the following equations:

$$\omega_{a1} = \omega_0 \frac{-\Omega_a\text{FBW} + \sqrt{(\Omega_a\text{FBW})^2 + 4}}{2} \tag{14a}$$

$$\omega_{a2} = \omega_0 \frac{\Omega_a\text{FBW} + \sqrt{(\Omega_a\text{FBW})^2 + 4}}{2}. \tag{14b}$$

In order to implement the abovementioned quasi-elliptic function filter in the form of microstrip, Fig. 12 describes the cou-
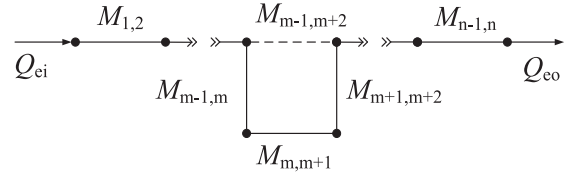

Fig. 12. General coupling structure of the BPFs with a single pair of TZs at finite frequencies.

pling structure of this type of filter, named CQ structure, in which each black point represents the resonator, the solid line represents the direct coupling between the two adjacent resonators, and the dash line indicates the cross coupling between the nonadjacent resonators.

According to the description in [47], the parameters of the filter coupling structure shown in Fig. 12 can be equivalent to the lowpass circuit prototype with the lumped-circuit elements. The relationship between the lowpass elements and the BPF parameters obtained by the J inverters as shown in the following equations:

$$Q_{ei} = Q_{eo} = \frac{g_1}{\text{FBW}} \tag{15}$$

$$M_{i,i+1} = M_{n-i,n-i+1} = \frac{\text{FBW}}{\sqrt{g_1 g_{i+1}}} \text{ for } i = 1 \text{ to } m-1 \tag{16}$$

$$M_{m,m+1} = \frac{\text{FBW} \cdot J_m}{g_m} \tag{17}$$

$$M_{m+1,m+2} = \frac{\text{FBW} \cdot J_{m-1}}{g_{m-1}} \tag{18}$$

where FBW represents the fractional bandwidth of the BPF; g represents the lumped-element value; J represents the transformed admittance characteristic value; n represents the order of the filter, and $m = n/2$; $M_{i,j}$ represents the coupling coefficient between the resonator i and j.

In order to achieve a pair of TZs at the specific frequencies, the coupling modes of $M_{m,m+1}$ and $M_{m-1,m+2}$ should be opposite (i.e., one is the electric coupling and the other is magnetic coupling), and the coupling modes of $M_{m-1,m}$ and $M_{m+1,m+2}$ should be the same (both electric or magnetic field coupling).

Under the weak-coupling condition, the four-order filter designed by the proposed Y-shape resonators is shown in Fig. 13(a). The electric cross coupling between the first and fourth resonators is introduced through a narrow cross-coupling microstrip line. According to the previous analysis of the coupling characteristics between the resonators, the dominant couplings between the yellow microstrip parts are the magnetic couplings, so it is known from the cross-coupling theory that a pair of TZs will be introduced at both sides of the Band I passband. For the green microstrip parts, according to the analysis of Fig. 5, the adjacent green parts are magnetic coupling, electric coupling, and magnetic coupling from left to right, respectively, so there is no a pair of TZs located outside the Band II passband. In Fig. 13(b), the frequency response curves with and without the cross coupling is depicted, and TZ$_1$ and TZ$_2$ are
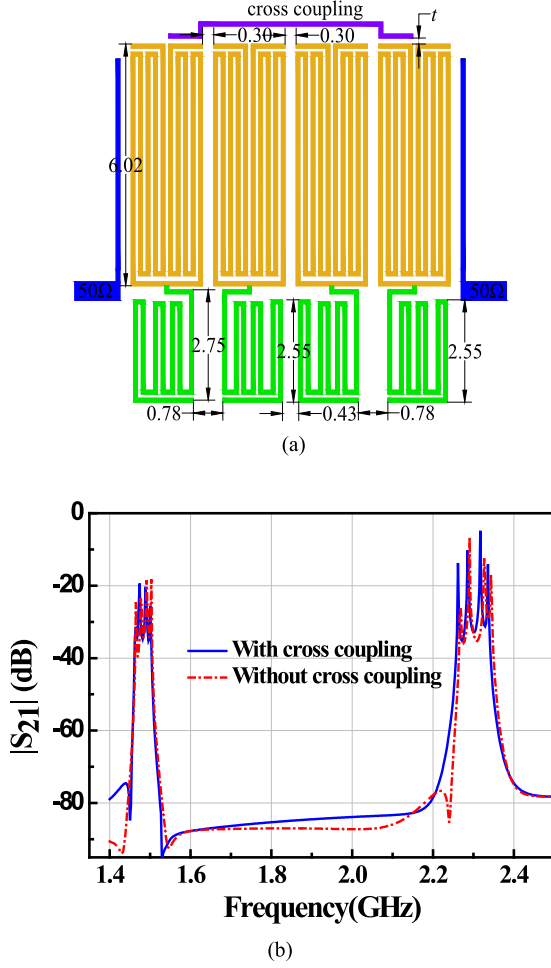
Fig. 13. Cross-coupling structure. (a) Four-order filter with cross coupling (unit: mm, t = 0.1). (b) Frequency responses.

located at 1446 and 1535 MHz, respectively, which obviously improves the roll-off characteristic of Band I. Note that there are two TZs introduced at passband I and one TZ generated at passband II before the narrow cross-coupling line is added. This is because for the filter layout shown in Fig. 13(a), without the cross-coupling line, the unnecessary coupling between nonadjacent resonators and the influence of external coupling can easily lead to phase change, which may affect the transmission characteristics outside the band and generate TZs. After introducing the cross-coupling line, TZs located at the passband I are closer to the center frequency and the roll-off characteristic is better, which proves that TZs at the passband I can be generated by adding the cross-coupling line.

IV. IMPLEMENTATION OF HTS DUAL-BAND FILTER

This section will use the topology shown in Fig. 12 to design a six-order ($n = 6$) HTS dual-band BPF with sharp roll-off and excellent insertion loss characteristics. The central frequencies of the two passbands are 1490 and 2340 MHz, respectively, and the bandwidths are 40 and 80 MHz, respectively. According to the Chebyshev prototype, the synthesized coupling coefficients are shown in Table I, in which $M_{i,j}$ represents the coupling

TABLE I
COUPLING COEFFICIENTS OF SIX-ORDER DUAL-BAND FILTER

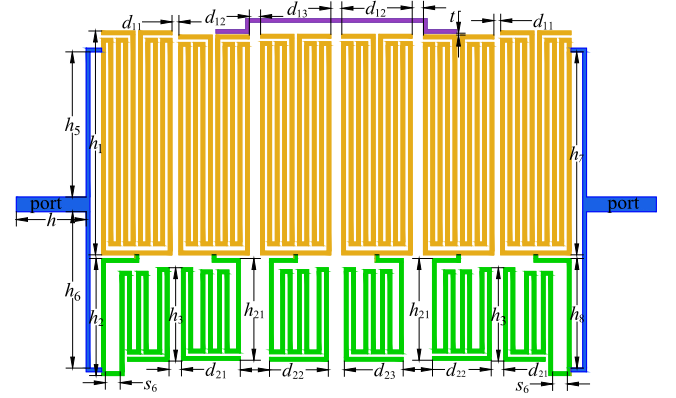| Bands	$M_{1,2} = M_{5,6}$	$M_{2,3} = M_{4,5}$	$M_{3,4}$	$M_{2,5}$	Q_e
Band I	0.023	0.018	0.015	-0.001	32.1
Band II	-0.025	0.019	-0.018	-0.002	28.8

Fig. 14. Layout of the designed six-order dual-band HTS filter.

coefficient between the resonators *i* and *j*. The negative values indicate the electric field coupling, and the positive ones indicate the magnetic field coupling.

On a double-sided YBCO/MgO/YBCO HTS substrate with a thickness of 0.5 mm and a dielectric constant 9.8, a dual-band CQ structure unit based on Fig. 13(a) and a direct-coupling tapped-line structure shown in Fig. 8 are used to design the six-order HTS dual-band filter, as shown in Fig. 14. The specific design process is summarized as follows: First, the values of h_1, h_2, and h_3 in Fig. 14 are adjusted to control the central frequencies of the filter, and $h_1 = 6.1$ mm, $h_2 = 3.2$ mm, $h_3 = 2.5$ mm, $h_{21} = 2.7$ mm, and $s_6 = 0.4$ mm are obtained. Second, according to the analysis of the two coupling types shown in Fig. 5, $d_{11} = 0.18$, $d_{12} = 0.29$, and $d_{13} = 0.30$ mm are adjusted to obtain the required coupling coefficients in Band I; the values of each resonator's s_4 and s_5 are varied so that the distances between the resonators are $d_{21} = 0.33$, $d_{22} = 0.78$, and $d_{23} = 0.43$ mm, which can satisfy the coupling coefficients required by Band II. Meanwhile, the couplings in Band I are almost invariable. Third, according to the analysis of Fig. 8, the widths of the parallel tapped lines with the length of h_5 and h_6 are set to be 0.1 mm, and the widths are chosen to be 0.4 mm in order to match the filter connectors. By adjusting $h_8 = 3.0$ and $h_7 = 5.5$ mm, the external quality factors of Bands II and I are satisfied ($Q_{e2} = 28.8$ and $Q_{e1} = 32.1$), and the fine tuning of $h_5 = 4.0$ and $h_6 = 4.2$ mm is made to further optimize Q_{e1} and Q_{e2}. Finally, through changing the distance t ($t = 0.05$ mm) between the cross-coupling line and the resonators, the demanded out-of-band rejection are achieved.

The electromagnetic simulation response curve of the HTS dual-band filter is shown in Fig. 16, and there are five TZs located at 1440, 1458, 1546, 2248 and 2510 MHz, respectively. Because of the existence of these TZs, the band-edge
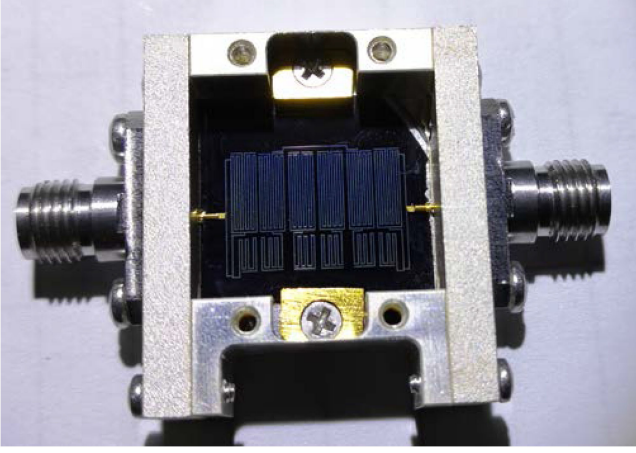
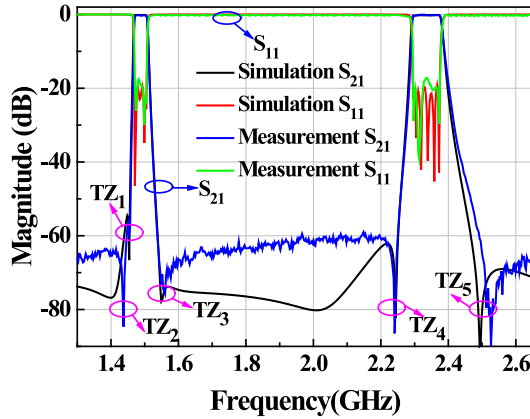Fig. 15.   Photograph of the fabricated HTS filter with connectors.

Fig. 16.   Simulated and measured results of HTS dual-band filter.

TABLE II
PERFORMANCE OF THE DUAL BAND FILTER

Frequency of band	ζ_{ROR} (dB/GHz)	Rejection (dB)
1470	4255	80
1510	2500	75
2300	1888	85
2380	1224	90
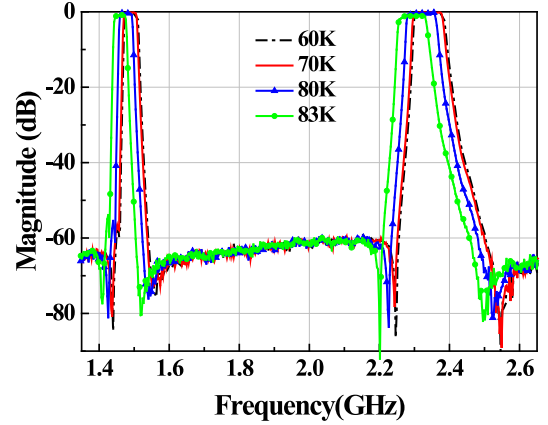
Fig. 17.   Measured frequency responses of dual-band HTS filter at different temperatures.

cut-off characteristics of the passbands are great, and the inhibition level between the two passbands is satisfying as well. The designed dual-band filter is fabricated on double-sided YBCO/MgO/YBCO HTS thin films with a size of 17.2 mm × 14.7 mm ($0.20\,\lambda_g$ × $0.17\,\lambda_g$, λ_g is the guided wavelength of the 50 Ω line in the substrate at the center frequency of the first passband), a thickness of 0.5 mm, and a dielectric constant of 9.8. One side of the HTS films is patterned into the filter circuit by the standard procedure of photolithography and ion etching, and the other side is used for grounding. The filter is then packaged in a metal shield box. Fig. 15 shows the photograph of the HTS dual-band filter.

At the temperature of 77 K, the HTS dual-band filter is tested by the dual-port vector network analyzer. The measured results are shown in Fig. 16, where it can be observed that the center frequencies are 1490 and 2340 MHz, respectively; the 3-dB bandwidths are 40 and 80 MHz, respectively; the maximum insertion losses in the passband are 0.20 and 0.25 dB, respectively, which can well reflect the low insertion loss characteristics of the HTS material. The return losses are better than that of 18.5 and 18.1 dB, respectively. The suppressions at the TZs' frequencies are greater than 70 and 80 dB, respectively. On the whole, the rejection levels and positions of TZs are in good agreement with the theoretical ones. The other small differences between the test

results and the simulated results are caused by the fabrication errors of the circuit and the film-making process, however, they are all within reasonable limits.

The formula of roll-off ratio is defined as (19), in which ζ_{ROR} indicates the roll-off ratio in band edge, δ_{-30dB} and δ_{-3dB} are the frequency response attenuations of 30 dB and 3 dB, respectively, and f_{-30dB} and f_{-3dB} are the frequencies corresponding to 30 and 3 dB losses.

$$\zeta_{ROR} = \frac{|\delta_{-30\,dB} - \delta_{-3\,dB}|}{|f_{-30\,dB} - f_{-3\,dB}|}. \tag{19}$$

According to the measured results shown in Fig. 16 and (19), the roll-off rates of the designed dual-band filter are calculated in Table II, where it can be seen that the selectivity of the filter is superior.

The double-sided HTS YBCO/MgO/YBCO thin film exhibits different microwave surface resistances at different temperatures, and the MgO substrate has varied dielectric constants with the change of the temperature. These characteristics changes will lead to the drift of frequency response curves and the variations of the insertion losses in the filter. Fig. 17 shows the S_{21} frequency response magnitude curves obtained at temperatures of 60, 70, 80, and 83 K. It can be seen that when the temperature is more than 83 K, the insertion losses of the dual-band filter becomes larger, which means the superconductivity is about to disappear. And when the temperature is below 70 K, the dielectric constant of the MgO substrate remains almost unchanged, and the frequency shift of the dual-band filter response curve is very slight, which is in accordance with the property of the YBCO\MgO\YBCO superconducting thin films.

V. CONCLUSION

In this paper, a HTS dual-band filter is designed. The filter can realize controllable center frequencies and bandwidths in two passbands by adjusting the proposed Y-shape resonators and the coupling distances between them. The two types of theory of controllable electric magnetic mixed coupling and cross coupling to create attenuation poles are introduced into the design of this dual-band filter, where TZs are produced in multiple outside the two passbands, and then can be independently controlled. Eventually, five TZs are generated at 1440, 1458, 1546, 2248, and 2510 MHz of the passband band edges. The test results are in good agreement with the simulated ones, which reflects the excellent selectivity and out-of-band suppression.

REFERENCES

[1] U. Naeem, A. Perigaud, and S. Bila, "Dual-mode dual-band bandpass cavity filters with widely separated passbands," *IEEE Trans. Microw. Theory Techn.*, vol. 65, no. 8, pp. 2681–2686, Aug. 2017.

[2] K. Zhou, C. Zhou, and W. Wu, "Substrate-integrated waveguide dual-mode," *IEEE Trans. Microw. Theory Techn.*, vol. 65, no. 10, pp. 3801–3812, Oct. 2017.

[3] X. Y. Zhang and Q. Xue, "Novel dual-mode dual-band filters using coplanar-waveguide-fed ring resonators," *IEEE Trans. Microw. Theory Techn.*, vol. 55, no. 10, pp. 2183–2190, Oct. 2007.

[4] F. Song, B. Wei, L. Zhu, B. Cao, and X. Lu, "Dual-band high-temperature superconducting bandpass filter using quint-mode stub-loaded resonators," *IEEE Trans. Appl. Supercond.*, vol. 25, no. 4, Aug. 2015, Art. no. 1501410.

[5] J. Xu, W. Wu, and G. Wei, "Novel dual-band bandpass filter and re-configurable filters using lumped-element dual-resonance resonators," *IEEE Trans. Microw. Theory Techn.*, vol. 64, no. 5, pp. 1496–1507, May 2016.

[6] A. Görür, "Description of coupling between degenerate modes of a dual-mode microstrip loop resonator using a novel perturbation arrangement and its dual-mode bandpass filter applications," *IEEE Trans. Microw. Theory Techn.*, vol. 52, no. 2, pp. 671–677, Feb. 2004.

[7] J. S. Hong, H. Shaman, and Y. H. Chun, "Dual-mode microstrip open-loop resonators and filters," *IEEE Trans. Microw. Theory Techn.*, vol. 55, no. 8, pp. 1764–1770, Aug. 2007.

[8] Q. X. Chu, F. C. Chen, Z. H. Tu, and H. Wang, "A novel crossed resonator and its applications to bandpass filters," *IEEE Trans. Microw. Theory Techn.*, vol. 57, no. 7, pp. 1753–1759, Jul. 2009.

[9] S. Luo, L. Zhu, and S. Sun, "A dual-band ring-resonator bandpass filter based on two pairs of degenerate modes," *IEEE Trans. Microw. Theory Techn.*, vol. 58, no. 12, pp. 3427–3432, Dec. 2010.

[10] X. Y. Zhang, C. H. Chan, Q. Xue, and B. J. Hu, "Dual-band bandpass filter with controllable bandwidths using two coupling paths," *IEEE Microw. Wireless Compon. Lett.*, vol. 20, no. 11, pp. 616–618, Nov. 2010.

[11] S. Sun, "A dual-band bandpass filter using a single dual-mode ring res-onator," *IEEE Microw. Wireless Compon. Lett.*, vol. 21, no. 6, pp. 298–300, Jun. 2011.

[12] H. Liu, B. Ren, X. Guan, J. Lei, and S. Li, "Compact dual-band band-pass filter using quadruple-mode square ring loaded resonator (SRLR)," *IEEE Microw. Wireless Compon. Lett.*, vol. 23, no. 4, pp. 181–183, Apr. 2013.

[13] J. M. Yan, L. Z. Cao, J. Xu, and R. S. Chen, "Design of a fourth-order dual-band bandpass filter with independently controlled external and inter-resonator coupling," *IEEE Microw. Wireless Compon. Lett.*, vol. 25, no. 10, pp. 642–644, Oct. 2015.

[14] M. L. Chuang and M. T. Wu, "Transmission zero embedded dual-band impedance transformer with three shunt stubs," *IEEE Microw. Wireless Compon. Lett.*, vol. 27, no. 9, pp. 788–790, Sep. 2017.

[15] G. Zhang, J. Wang, L. Zhu, and W. Wu, "Dual-band filtering power divider with high selectivity and good isolation," *IEEE Microw. Wireless Compon. Lett.*, vol. 26, no. 10, pp. 774–776, Dec. 2016.

[16] J. Xu, Z. Chen, and Q. Cai, "Design of miniaturized dual-band low-pass–Bandpass and bandpass filters," *IEEE Trans. Compon. Packag. Manuf. Technol.*, vol. 8, no. 1, pp. 132–139, Jan. 2018.

[17] Y. Peng, L. Zhang, Z. Zheng, and Y. Leng, "High selective compact dual-band filter using ring resonator with quarter-wavelength stubs," *Electron. Lett.*, vol. 53, no. 24, pp. 1589–1591, Nov. 2017.

[18] V. K. Killamsetty and B. Mukherjee, "Compact dual bandpass filter for terrestrial radio and GSM applications," *Int. J. RF Microw. Comput.-Aided Eng.*, vol. 27, no. 8, pp. 1–8, May 2017.

[19] H. Liu *et al.*, "Dual-band high-temperature superconducting hairpin-resonator bandpass filter based on two pairs of nondegenerate modes," *IEEE Trans. Appl. Supercond.*, vol. 25, no. 3, Jun. 2015, Art. no. 1500104.

[20] X. Y. Zhang, J. X. Chen, Q. Xue, and S. M. Li, "Dual-band bandpass filters using stub-loaded resonators," *IEEE Microw. Wireless Compon. Lett.*, vol. 17, no. 8, pp. 583–585, Aug. 2007.

[21] H. Liu, B. Ren, X. Guan, P. Wen, and Y. Wang, "Quad-band higherature superconducting bandpass filter using quadruple-mode square ring loaded resonator," *IEEE Trans. Microw. Theory Techn.*, vol. 62, no. 12, pp. 2931–2941, Dec. 2014.

[22] M.-Q. Zhou, X.-H. Tang, and F. Xiao, "Design of compact dual band bandpass filter with controllable bandwidths and good selectivity," in *Proc. IEEE MTT-S Int. Microw. Workshop Ser. Art Miniaturizing RF Microw. Passive Compon.*, Dec. 2008,vol. 18, no. 12, pp. 145–148.

[23] H. Liu *et al.*, "Dual-band superconducting bandpass filter using embedded split ring resonator," *IEEE Trans. Appl. Supercond.*, vol. 23, no. 3, Jun. 2013, Art. no. 1300304.

[24] H. Liu, F. Liu, F. Qin, B. Ren, P. Wen, and X. H. Guan, "Compact dual-band HTS bandpass filter using spirally asymmetric stepped-impedance resonators," *IEEE Trans. Appl. Supercond.*, vol. 26, no. 7, Oct. 2016, Art. no. 1501805.

[25] J. T. Kuo, T. H. Yeh, and C. C. Yeh, "Design of microstrip bandpass filters with a dual-passband response," *IEEE Trans. Microw. Theory Techn.*, vol. 53, no. 4, pp. 1331–1337, Apr. 2005.

[26] L. M. Wang *et al.*, "Quarter-wavelength stepped-impedance YBCO res-onators for miniaturized dual-band high-Tc superconducting filters," *IEEE Trans. Appl. Supercond.*, vol. 19, no. 3, pp. 895–898, Jun. 2009.

[27] Y. T. Kuo and C. Y. Chang, "Analytical design of two-mode dual-band filters using E-shaped resonators," *IEEE Trans. Microw. Theory Techn.*, vol. 60, no. 2, pp. 250–260, Feb. 2012.

[28] Y. Heng *et al.*, "Dual-band superconducting bandpass filter using stub-loaded resonators with controllable coupling and feeding structures," *IEEE Microw. Wireless Compon. Lett.*, vol. 23, no. 8, pp. 400–402, Aug. 2013.

[29] Y. Heng *et al.*, "Dual-band superconducting bandpass filter with embedded resonator structure," *Electron. Lett.*, vol. 49, no. 17, pp. 1096–1097, Aug. 2013.

[30] Z. Xu *et al.*, "A compact dual-band bandpass superconducting filter using microstrip/CPW spiral resonators," *IEEE Microw. Wireless Compon. Lett.*, vol. 23, no. 11, pp. 584–586, Nov. 2013.

[31] N. Sekiya and S. Sugiyama, "Design of miniaturized HTS dual-band bandpass filters using stub-loaded meander line resonators and their ap-plications to tri-band bandpass filters," *IEEE Trans. Appl. Supercond.*, vol. 25, no. 3, pp. 3–7, Jun. 2015.

[32] H. Liu, B. Ren, F. Liu, X. Guan, P. Wen, and Z. Ma, "Dual-band high-temperature superconducting bandpass filter using dual-mode hairpin ring resonator," *IEEE Trans. Appl. Supercond.*, vol. 26, no. 7, Oct. 2016, Art. no. 1501704.

[33] F. Song, B. Wei, L. Zhu, Y. Feng, R. Wang, and B. Cao, "A novel tri-band superconducting filter using embedded stub-loaded resonators," *IEEE Trans. Appl. Supercond.*, vol. 26, no. 8, Dec. 2016, Art. no. 1502009.

[34] N. Sekiya, "Design of compact HTS dual-band bandpass filters using dual-function feeding structure with wide stop-band response," *IEEE Trans. Appl. Supercond.*, vol. 27, no. 1, pp. 10–13, Jan. 2017.

[35] P. Ma, B. Wei, J. Hong, B. Cao, X. Guo, and L. Jiang, "Design of dual-mode dual-band superconducting filters," *IEEE Trans. Appl. Supercond.*, vol. 27, no. 7, Oct. 2017, Art. no. 1502809.

[36] X. Chen, L. Zhang, C. Xu, Z. Zheng, and X. Jiang, "Dual-band filter syn-thesis based on two low-pass prototypes," *IEEE Microw. Wireless Compon. Lett.*, vol. 27, no. 10, pp. 903–905, Oct. 2017.

[37] L. Szydlowski, N. Leszczynska, and M. Mrozowski, "Generalized Cheby-shev bandpass filters with frequency-dependent couplings based on stubs," *IEEE Trans. Microw. Theory Techn.*, vol. 61, no. 10, pp. 3601–3612, Oct. 2013.

[38] C. K. Liao, P. L. Chi, and C. Y. Chang, "Microstrip realization of gen-eralized Chebyshev filters with box-like coupling schemes," *IEEE Trans. Microw. Theory Techn.*, vol. 55, no. 1, pp. 147–153, Jan. 2007.

[39] T. Yu *et al.*, "A novel quasi-elliptic HTS filter with group-delay equaliza-tion using compact quasi-lumped element resonators in VHF band," *IEEE Trans. Appl. Supercond.*, vol. 19, no. 2, pp. 69–75, Apr. 2009.

[40] I. B. Vendik *et al.*, "Narrowband Y-Ba-Cu-O filter with quasi-elliptic characteristic," *IEEE Trans. Appl. Supercond.*, vol. 11, no. 1, pp. 477–480, Mar. 2001.

[41] J. Hong, M. J. Lancaster, D. Jedamzik, R. B. Greed, J. Mage, and A. Member, "On the performance of HTS microstrip quasi-elliptic function filters for application," *IEEE Trans. Microw. Theory Techn.*, vol. 48, no. 7, pp. 1240–1246, Jul. 2000.

[42] H. Wang and Q. X. Chu, "Generation of transmission zero through electric and magnetic mixed coupling," in *Proc. Int. Conf. Microw. Millim. Wave Technol.*, Jul. 2007, pp. 1–3.

[43] Q. X. Chu and H. Wang, "A compact open-loop filter with mixed electric and magnetic coupling," *IEEE Trans. Microw. Theory Techn.*, vol. 56, no. 2, pp. 431–439, Feb. 2008.

[44] H. Wang and Q. X. Chu, "An EM-coupled triangular open-loop filter with transmission zeros very close to passband," *IEEE Microw. Wireless Compon. Lett.*, vol. 19, no. 2, pp. 71–73, Feb. 2009.

[45] H. Wang and Q. X. Chu, "An inline coaxial quasi-elliptic filter with controllable mixed electric and magnetic coupling," *IEEE Trans. Microw. Theory Techn.*, vol. 57, no. 3, pp. 667–673, Mar. 2009.

[46] J. C. Lu, C. K. Liao, and C. Y. Chang, "Microstrip parallel-coupled filters with cascade trisection and quadruplet responses," *IEEE Trans. Microw. Theory Techn.*, vol. 56, no. 9, pp. 2101–2110, Sep. 2008.

[47] J. S. Hong and M. J. Lancaster, "Design of highly selective microstrip bandpass filters with a single pair of attenuation poles at finite frequencies," *IEEE Trans. Microw. Theory Techn.*, vol. 48, no. 7, pp. 1098–1107, Jul. 2000.

Hui Li (M'06) received the M.S. and Ph.D. degrees from Northwestern Polytechnical University, Xi'an, China, in 1987 and 1991, respectively.

He is currently a Professor and the Associate Dean with the School of Aeronautics and Astronautics, University of Electronic Science and Technology of China, Chengdu, China. His research interests include the spacecraft simulation and fault diagnosis, space launching technology, intelligent mechanical electrical systems, and power electronics.

Dr. Li is a System Simulation Member of the Chinese Society of Automation and a member of China Aerospace and Association.

Zhihe Long, biography not available at the time of publication.

Shuangshuang Cao, biography not available at the time of publication.

Mingyan Jiang, biography not available at the time of publication.

Liguo Zhou was born in July 1987. He received the M.S. degree in 2016 from the School of Astronautics and Aeronautics, University of Electronic Science and Technology, Chengdu, China, where he is currently working toward the Ph.D. degree in navigation, guidance and control.

His research interests include application technology of high-temperature superconductors and radio frequency and microwave technology.

Tianliang Zhang (M'12) was born in August 1976. He received the M.S. and Ph.D. degrees in physical electronics from the University of Electronic Science and Technology of China (UESTC), Chengdu, China, in 2004 and 2009, respectively.

He is currently a Full-Time Professor with UESTC. His research interests include high-temperature superconducting microwave circuits and systems, CAD, CAA, and production technology of high-temperature superconducting microwave circuits.